GEOPHYSICS, VOL. 77, NO. 4 (JULY-AUGUST 2012); P. WB127–WB135, 7 FIGS.
10.1190/GEO2011-0379.1

Estimating source locations of unexploded ordnance using the multiple signal classification algorithm

Lin-Ping Song[1], Douglas W. Oldenburg[1], and Leonard R. Pasion[2]

ABSTRACT

To extract intrinsic polarization parameters of a buried object from electromagnetic induction (EMI) responses, one has to first find its location. We developed an efficient method to find the approximate locations of multiple ordnance items using time domain electromagnetic data. The procedure was based upon the principle of multiple signal classification which exploits the orthogonality of signal and noise subspaces of multistatic EMI data. For an arbitrary multistatic array, we formulated transmitter-based and receiver-based imaging or steering vectorial operators that related with the left and right singular vectors of a multistatic response matrix. The operators were computed at potential source locations and are mapped onto the noise subspaces derived from data. A spatial metric function was therefore introduced to measure the magnitude of the projection. A 3D source imaging of the metric function could be obtained by evaluating all potential locations over a region of interest. In ideal cases, the perfect orthogonality between the computed signal subspace and measured noisy subspace can be achieved at or near a target location, and rendered an imaging peak at that location. Conversely, the peak image locations obtained from this technique were used as the indicators for where targets were most likely present. The number of targets could be estimated from the rank of the data matrix, provided there were a sufficient number of transmitters and receivers. In some instances the locations of multiple targets were imaged directly, but the procedure was enhanced by stripping the effect of a larger or shallower target from the image. The technique was evaluated using the test-stand and field data, and compared with the standard nonlinear inversion. The results showed that it has potential capability to accurately localize sources in EMI sensing.

INTRODUCTION

The source localization problem arises when using an electromagnetic induction (EMI) sensor to detect objects and discriminate unexploded ordnance (UXO) from clutter (Das et al., 1990; Bell et al., 2001; Pasion and Oldenburg, 2001; Zhang et al., 2003; Smith and Morrison, 2004; Pasion, 2007; Beran and Oldenburg, 2008; Snyder et al., 2008; Gasperikova et al., 2009; Billings et al., 2010). To accurately extract polarization tensor parameters from the EMI response, we need reasonably accurate estimates of the location of the source. We also need to decide if the observed anomaly is due to a single object or two or more objects (Bell, 2006; Grzegorczyk et al., 2009; Song et al., 2009; Miller et al., 2010; Shubitidze et al., 2010; Song et al., 2011). Recent advances in EMI instrumentation have produced systems that are able to acquire multistatic/multicomponent data. Full exploitation of such data sets necessitates the development of new signal processing techniques. In this paper, we present a new 3D imaging technique for EMI source detection and localization using the idea of multiple signal classification (MUSIC) (Schmidt, 1986).

The MUSIC algorithm proposed by Schmidt (1986) is based upon the orthogonal property of a signal subspace and a noise subspace contained in a data matrix. A metric which measures the degree of orthogonality is used to search for sources. This technique has been extensively investigated in radar and acoustics for estimating directions or locations of multiple sources (Krim and Viberg, 1996). Recently Devaney (2005), using a multistatic radar antenna array, combined time-reversal methods and the MUSIC algorithm to image hidden targets.

Manuscript received by the Editor 4 October 2011; revised manuscript received 27 February 2012; published online 9 July 2012.
[1]University of British Columbia, Department of Earth and Ocean Sciences, Vancouver, BC, Canada. E-mail: lpsong@eos.ubc.ca; doug@eos.ubc.ca.
[2]Sky Research Inc., Vancouver, BC, Canada. E-mail: len.pasion@skyresearch.com.

When using electromagnetics for UXO problems, the standard processing method of finding buried sources is to formulate a nonlinear data-fitting optimization problem that is solved for source location and polarizations of the UXO from an initial model (Pasion and Oldenburg, 2001; Smith and Morrison, 2004; Bell, 2006; Grzegorczyk et al., 2009; Song et al., 2009; Shubitidze et al., 2010; Song et al., 2011). However, the problem of finding source location can be completely separated from the estimation of polarization spectra. Once the source location is determined, the estimation of source polarization in principle reduces to the problem of a simple linear least-squares fit. For example, Shubitidze et al. (2007) proposes a method of combining total normalized surface magnetic charge model (NSMC) with a pseudospectral finite difference (PSFD) method for localizing a buried object. (Song et al., 2008) adapt a beamforming technique (Van Veen and Buckley, 1988) to localize sources using traditional monostatic measurements (i.e., transmitters and receivers are colocated).

New-generation EMI instruments have multiple transmitters and multiple receivers. Each transmitter is fired independently, and data are recorded at all of the receivers. This results in a richer and more coherent data matrix than could be obtained from monostatic equipment. As in the radar case (Devaney, 2005), we expect that by combining the multistatic response measurements and the MUSIC principle an improved technique might be obtained, compared to the standard one (Pasion and Oldenburg, 2001; Smith and Morrison, 2004; Bell, 2006; Grzegorczyk et al., 2009; Song et al., 2009; Shubitidze et al., 2010; Song et al., 2011).

In this paper, we present the theory and formulation of our MUSIC imaging technique for an EMI sensor array, by dealing with vectorial magnetic fields, the polarization tensor, and wideband responses. Then we evaluate the MUSIC algorithm using the test-stand and field data collected with the TEMTADS (Nelson, 2008) and MetalMapper (Snyder et al., 2010) systems, and compare and contrast its performance with the standard nonlinear inversion techniques.

THE DATA MODEL

Consider a standard EMI system consisting of a transmitting coil and a receiving coil; they may be colocated or not. In active sensing, a primary field emitted from a transmitter illuminates the subsurface and its changes with time-induced eddy currents in the metal object. These induced currents produce a transient secondary magnetic field that is measured by a receiver. In practice, an array of sensors is generally positioned above the surface. For a UXO survey where the target dimension is often small relative to the target-sensor distance, the primary fields around the target are approximately uniform and the induced eddy currents in the target are localized and predominantly produce dipole responses (Grant and West, 1965; Jackson, 1975). The EMI nature of a metal target generally can be well represented by an equivalent induced dipole. Here we assume that dipole location and orientation are independent of time. If the target location is denoted by $\mathbf{r}$ then the induced dipole moment $\mathbf{m}(t)$ at time t is represented by (Das et al., 1990; Pasion and Oldenburg, 2001; Smith and Morrison, 2004)

$$\mathbf{m}(t) = P(t)\mathbf{B}_T(\mathbf{r}, \mathbf{r}_{Tx}), \tag{1}$$

where $\mathbf{B}_T$ is the exciting magnetic field vector at the target location from a transmitter at $\mathbf{r}_{Tx}$ and $P(t)$ is a 3×3 symmetric magnetic polarizability tensor (MPT)

$$P(t) = \begin{bmatrix} p_{11}(t) & p_{12}(t) & p_{13}(t) \\ p_{12}(t) & p_{22}(t) & p_{23}(t) \\ p_{13}(t) & p_{23}(t) & p_{33}(t) \end{bmatrix}. \tag{2}$$

Physically, the element $p_{ij}(t)$ of the tensor $P(t)$ represents a dipole component in the ith Cartesian direction due to a primary field in jth Cartesian direction. This polarizability tensor $P(t)$ has an eigen decomposition as

$$P(t) = EL(t)E', \tag{3}$$

where E is the orthonormal matrix whose columns refer to principal directions of dipolar polarization with respect to a reference system, and $L_{ii}(t)$ of the diagonal matrix $L(t)$ is the principal polarization strength that is a function of the geometry and material of a target. The prime denotes a transpose. $P(t)$ contains the information regarding the geometry and material of a target as well as its orientation. The secondary response d_{ij} due to a target at $\mathbf{r}$ is given by (Das et al., 1990; Miller et al., 2001; Smith and Morrison, 2004; Song et al., 2011)

$$d_{ij}(\mathbf{r}_{Rx_i}, \mathbf{r}_{Tx_j}, t) = \mathbf{B}_R'(\mathbf{r}, \mathbf{r}_{Rx_i})P(t)\mathbf{B}_T(\mathbf{r}, \mathbf{r}_{Tx_j}), \tag{4}$$

where $\mathbf{B}_R(\mathbf{r}, \mathbf{r}_{Rx_i})$ and $\mathbf{B}_T(\mathbf{r}, \mathbf{r}_{Tx_i})$ are the field vectors at target location $\mathbf{r}$ generated by the ith receiver and the jth transmitter. Equation 4 describes the basic EMI process of illuminating, scattering, and sensing. It is the model from which we begin our formulation of the MUSIC imaging methodology.

MULTISTATIC RESPONSE MATRIX AND THE SVD

For an array consisting of M receivers and N transmitters, i.e., $i = 1 \cdots M$, $j = 1 \cdots N$, we can arrange the measured responses at time t as

$$D(t) = \begin{bmatrix} d_{11}(t) & \dots & d_{1N}(t) \\ \vdots & \vdots & \vdots \\ d_{M1}(t) & \dots & d_{MN}(t) \end{bmatrix}. \tag{5}$$

We call this the "multistatic response matrix" (MRM). A row corresponds to measurements from the same receiver due to different excitations (a transmitter array) and a column corresponds to measurements from different receivers (a receiver array) due to the same excitation.

Taking the singular value decomposition (SVD) (Horn and Johnson, 1985; Golub and Loan, 1989) of D in Equation 5, yields

$$D(t) = U\Sigma V' = \sum_{i=1}^{p} \sigma_{ii}\mathbf{u}_i\mathbf{v}_i', \tag{6}$$

where $p = \min(M, N)$, $U = [\mathbf{u}_1, \cdots, \mathbf{u}_M]$ is an $M \times M$ orthonormal matrix and $V = [\mathbf{v}_1, \cdots, \mathbf{v}_N]$ is an $N \times N$ orthonormal matrix, and Σ is an $M \times N$ matrix with elements σ_{ii} along the diagonal and zeros everywhere else. The matrix U is called the "left singular matrix," V is called the "right singular matrix," and Σ is the "singular value matrix." If the singular values are ordered so that,

$$\sigma_{11} \geq \sigma_{22} \geq \cdots \ \sigma_{pp} \geq 0 \tag{7}$$

and if the matrix has a rank $r < p$, then the last singular values are equal to zero, and the SVD of D becomes

$$D(t) = \sum_{i=1}^{r} \sigma_{ii} \mathbf{u}_i \mathbf{v}_i'. \tag{8}$$

Next, we interpret the singular values and the corresponding singular vectors with the principal polarizabilities of an object and the vectorial fields in equation 4.

Array Green's functions and the SVD

To make the following derivation simple, we consider a single-object case. Recall that equation 4 represents a mathematical expression for the measured EMI response to a single object when using a single transmitter and a single receiver. Replacing each entry in equation 5 with equation 4, we have

$$\begin{aligned} D(t) &= \begin{bmatrix} \mathbf{B}_R'(\mathbf{r}, \mathbf{r}_{Rx_1}) P(t) \mathbf{B}_T(\mathbf{r}, \mathbf{r}_{Tx_1}) & \cdots & \mathbf{B}_R'(\mathbf{r}, \mathbf{r}_{Rx_1}) P(t) \mathbf{B}_T(\mathbf{r}, \mathbf{r}_{Tx_N}) \\ \vdots & \vdots & \vdots \\ \mathbf{B}_R'(\mathbf{r}, \mathbf{r}_{Rx_M}) P(t) \mathbf{B}_T(\mathbf{r}, \mathbf{r}_{Tx_1}) & \cdots & \mathbf{B}_R'(\mathbf{r}, \mathbf{r}_{Rx_M}) P(t) \mathbf{B}_T(\mathbf{r}, \mathbf{r}_{Tx_N}) \end{bmatrix} \\ &= \begin{bmatrix} \mathbf{B}_R'(\mathbf{r}, \mathbf{r}_{Rx_1}) \\ \vdots \\ \mathbf{B}_R'(\mathbf{r}, \mathbf{r}_{Rx_M}) \end{bmatrix} P(t) \left[\mathbf{B}_T(\mathbf{r}, \mathbf{r}_{Tx_1}) \quad \cdots \quad \mathbf{B}_T(\mathbf{r}, \mathbf{r}_{Tx_N}) \right]. \end{aligned} \tag{9}$$

Setting

$$G_{Rx} = \begin{bmatrix} \mathbf{B}_R'(\mathbf{r}, \mathbf{r}_{Rx_1}) \\ \vdots \\ \mathbf{B}_R'(\mathbf{r}, \mathbf{r}_{Rx_M}) \end{bmatrix}, \qquad G_{Tx} = \begin{bmatrix} \mathbf{B}_T'(\mathbf{r}, \mathbf{r}_{Tx_1}) \\ \vdots \\ \mathbf{B}_T'(\mathbf{r}, \mathbf{r}_{Tx_N}) \end{bmatrix}, \tag{10}$$

then we have

$$D(t) = G_{Rx} P(t) G_{Tx}', \tag{11}$$

where $G_{Rx} \in \mathbb{R}^{M \times 3}$ is the Green's function matrix of a receiver array and $G_{Tx} \in \mathbb{R}^{N \times 3}$ is the Green's function matrix of a transmitter array. Viewed as a mapping process from the transmitter to receiver space, D is spatially characterized by the two array functions G_{Rx} and G_{Tx}.

Equation 11 is of similar form to the SVD of equation 6. It implies that there are correspondences between the array Green's functions and the left and right singular vectors. To elaborate this, we introduce two additional weighting matrices (Horn and Johnson, 1985)

$$W_{Rx} = (G_{Rx}' G_{Rx})^{\frac{1}{2}}, \qquad W_{Tx} = (G_{Tx}' G_{Tx})^{\frac{1}{2}}. \tag{12}$$

Using W_{Rx} and W_{Tx}, we can rewrite equation 11 as

$$D(t) = (G_{Rx} W_{Rx}^{-1}) W_{Rx} P(t) W_{Tx} (G_{Tx} W_{Tx}^{-1})'. \tag{13}$$

To facilitate the discussion, we set

$$U_{Rx} = G_{Rx} W_{Rx}^{-1}, \quad V_{Tx} = G_{Tx} W_{Tx}^{-1}, \quad \Omega = W_{Rx} P(t) W_{Tx}, \tag{14}$$

where U_{Rx} and V_{Tx} have orthonormal columns, i.e., $U_{Rx}' U_{Rx} = I_3$ and $V_{Tx}' V_{Tx} = I_3$, and Ω can be viewed as the weighted polarizability tensors. Taking the SVD of Ω, $\Omega = U_\Omega \Lambda V_\Omega'$, we can derive an orthonormalized version of equation 11

$$D(t) = U_{Rx} U_\Omega \Lambda (V_{Tx} V_\Omega)'. \tag{15}$$

What we see is that equation 15 is an exact SVD representation of the data matrix D, and that it will have three nonzero eigenvalues. In other words, it shows that the rank r is equal to three for a single-object case. Its left and right singular vectors are the columns of the matrix $U_{Rx} U_\Omega$ and the matrix $V_{Tx} V_\Omega$, respectively. The nonzero singular values of D are the diagonal entries of Λ, i.e., the eigenvalues of the weighted polarizability tensor Ω. The diagonal matrix Λ is related to the principal polarizabilities L as

$$\Lambda(t) = U_\Omega' W_{Rx} E L(t) E' W_{Tx} V_\Omega. \tag{16}$$

For perfect data, the two SVDs in equations 15 and 8 are identical and the rank of D will be three if there is a single object. Therefore, equation 16 explains that the singular values derived from measured data are the combination of the intrinsic target polarization and its orientation and field strength and may be regarded as the apparent target strengths or apparent principal polarizabilities. By equating the singular vectors in the two SVDs,

$$G_{Rx}(W_{Rx}^{-1} U_{\Omega,i}) = \mathbf{u}_i \quad G_{Tx}(W_{Tx}^{-1} V_{\Omega,i}) = \mathbf{v}_i \quad i = 1, \cdots, 3, \tag{17}$$

where $U_{\Omega,i}$ and $V_{\Omega,i}$ represent the ith column of U_Ω and V_Ω. We see that for $\sigma_{ii} > 0$ the singular vector $\mathbf{u}_i$ are the linear combinations of the receiver array Green's function matrix G_{Rx} and form an orthornormal basis for receiver array space, while the singular vectors $\mathbf{v}_i$ are linear combinations of the orthornormalized transmitter array Green's function matrix G_{Tx} and form an orthornormal basis for transmitter array space. Left and right singular vectors in the data contain information of the target location and can be used to find sources.

If there are η objects, we replace $P(t)$ in equation 11 with a $3\eta \times 3\eta$ block diagonal matrix, i.e, diagonal $(P_1, \cdots, P_\eta)$, where P_i, $(i = 1, \cdots, \eta)$ is a polarizability tensor of the ith object. Then the above analysis is similarly applied to a general case of multiple objects.

MUSIC

Assuming that the matrix has a rank r, as described in equation 8, we can group these SVD-constructed orthonormal vectors into the left and right signal subspaces, i.e., $U_s = [\mathbf{u}_1, \cdots, \mathbf{u}_r]$ and $V_S = [\mathbf{v}_1, \cdots, \mathbf{v}_r]$. The remaining singular vectors, $U_n = [\mathbf{u}_{r+1}, \cdots, \mathbf{u}_M]$ and $V_n = [\mathbf{v}_{r+1}, \cdots, \mathbf{v}_M]$, are correspondingly grouped as the left and right orthonormal noise subspaces. The left and right singular vectors in the signal subspace are related with 3C fields generated from receiver and transmitter at a location where a target is present. Because the fields in the problem are vectorial, and those signal space vectors are linear combinations of the fields, as shown in 17, we cannot relate a singular vector with a component field for a source detection or localization.

From the orthogonal property between the signal and noise subspaces, we expect that the projection of array Green's functions in the signal subspace onto the noise subspaces spanned by U_n and V_n will be zero. Namely, given the orthogonal projectors onto the receiver and transmitter noise spaces as

$$P_u^{\perp} = \sum_{i=r+1}^{M} \mathbf{u}_i\mathbf{u}_i' = U_nU_n', \qquad P_v^{\perp} = \sum_{i=r+1}^{N} \mathbf{v}_i\mathbf{v}_i' = V_nV_n', \tag{18}$$

then

$$P_u^{\perp}G_{Rx} = 0, \qquad P_v^{\perp}G_{Tx} = 0. \tag{19}$$

Due to various approximations and errors from the modeling, in particular an incorrect estimate of the target location, the projection might not be zero as suggested by equation 19. To evaluate the magnitude of array Greens's functions $G_{Rx}(\mathbf{r})$ and $G_{Tx}(\mathbf{r})$ lying on the noise subspace and consider their vectorial nature, we introduce a function,

$$\mathcal{S}(\mathbf{r}) = \sum_{i=1}^{3} \frac{\|G_{Rx,i}(\mathbf{r})\|^2}{\|P_u^{\perp}G_{Rx,i}(\mathbf{r})\|^2} \times \sum_{i=1}^{3} \frac{\|G_{Tx,i}(\mathbf{r})\|^2}{\|P_v^{\perp}G_{Tx,i}(\mathbf{r})\|^2}, \tag{20}$$

to measure the size of such projections. The denominators are the Frobenius norms of the projections of components $G_{Rx,i}(\mathbf{r})$ and $G_{Tx,i}(\mathbf{r})$ onto each individual noise subspace. We use a multiplication between the G_{Rx}- and G_{Tx}-related terms to enhance imaging ability. By varying $\mathbf{r}$, we would expect that $\mathcal{S}(\mathbf{r})$ peaks at or near a target location where $G_{Rx}(\mathbf{r})$ and $G_{Tx}(\mathbf{r})$ are largely in the signal subspace. This is a MUSIC-type functional or spatial spectrum for source imaging or localization.

The MRM-based imaging technique is, in principle, applicable to arbitrary sensor array geometries, but requires that the number of *Tx* and/or *Rx* be larger than the number of dipolar polarizations that need to be resolved. Equation 20 is designed for the case in which receiver and transmitter noise subspaces exist and can be used for a sensor system that has multiple transmitters and receivers like the TEMTADS (Nelson, 2008). For the case where there exists only the receiver noise subspace, like a sensor system that consists of multiple receivers but a few transmitters, e.g., the Berkeley UXO discriminator (Gasperikova et al., 2009), and MetalMapper (Snyder et al., 2010), equation 20 can be used just with $P_u^{\perp}$ term. Similarly, if there is only the transmitter noise subspace, like a sensor system that has multiple transmitters but a few receivers, equation 20 can be used with only the $P_v^{\perp}$ term.

For multisource detection, a strong target or shallow one can mask a weak or a deep target. To automatically detect all possible sources in various situations, we can eliminate the contribution of the first detected source $\mathbf{r}_1$ from the signal subspace by applying the projectors $P_{G_{R_x},1}^{\perp}$ to $G_{Rx}(\mathbf{r})$ and $P_{G_{T_x},1}^{\perp}$ to $G_{Tx}(\mathbf{r})$ in a second MUSIC search, where $P_{G_{R_x},1}^{\perp} = I - G_{Rx}(\mathbf{r}_1)[G_{Rx}'(\mathbf{r}_1)G_{Rx}(\mathbf{r}_1)]^{-1}G_{Rx}'(\mathbf{r}_1)$ and $P_{G_{T_x},1}^{\perp} = I - G_{Tx}(\mathbf{r}_1)[G_{Tx}'(\mathbf{r}_1)G_{Tx}(\mathbf{r}_1)]^{-1}G_{Tx}'(\mathbf{r}_1)$. As a result, the quantities of the numerators in equation 20 are replaced with $P_{G_{R_x},1}^{\perp}G_{Rx}(\mathbf{r})$ and $P_{G_{R_x},1}^{\perp}G_{Rx}(\mathbf{r})$. This process can be applied continually, and is equivalent to a subtraction of the known source contribution from the data.

Having obtained the object locations from the imaging, we can compute the principal polarizations for the objects by solving a constrained linear least-squares problems (Song et al., 2011).

Multichannel wideband responses: Joint diagonalization

So far, all discussions and the singular vector fields are based on an MRM at a single time. We might obtain a series of imaging snapshots by applying the MUSIC functional of equation 20 to MRMs at certain time channels and get an average of these images.

Instead, we can find common singular vectors across a range of times using a joint diagonalization technique (Cardoso and Souloumiac, 1996; Wax and Sheinvald, 1997). Assume a set of real-valued symmetric matrices $\{C_1, \ldots, C_K\}$ of size $q \times q$. The goal of a joint diagonalization algorithm is to find a best orthogonal transformation Y that in some sense "diagonalizes" all the given matrices: $C_1 = Y\tilde{\Sigma}_1Y', \cdots, C_K = Y\tilde{\Sigma}_KY'$, where $\tilde{\Sigma}_1, \cdots, \tilde{\Sigma}_K$ are found as $q \times q$ diagonal matrices. Y represents an average eigen structure shared by the matrices $C_1, \cdots, C_K$. In our imaging application of the joint diagonalization method, the common left and right singular matrices are used rather than those obtained at each time channel. Generally, there is no guarantee that the MRM is square and symmetric and we cannot directly apply the joint diagonalization method to the MRM. However, from the SVD representation in equation 6 we know that the columns of V make up the eigenvectors of $D'D$, and the columns of U are the eigenvectors of DD'; i.e.,

$$D'D\mathbf{v}_i = \sigma_i^2\mathbf{v}_i \quad DD'\mathbf{u}_i = \sigma_i^2\mathbf{u}_i. \tag{21}$$

Therefore, we can form $C_1 = D_1'D_1, \cdots, C_K = D_K'D_K$ to obtain the common set of the right singular vectors $\mathbf{v}_i$ and $C_1 = D_1D_1', \cdots, C_K = D_KD_K'$ the common set of the left singular vectors $\mathbf{u}_i$. Then these average singular vectors are used in the MUSIC imaging to localize the objects.

The MUSIC is a noniterative method to find a source in contrast to a standard nonlinear inversion algorithm. Its main computation of equation 20 is the construction of array Green's functions $G_{R_x}(r)$ and $G_{R_x}(r)$ over a 3D grid. Its algorithm complexity is on the order of $\mathcal{O}(ML_g) + \mathcal{O}(NL_g)$, where L_g is the number of a 3D grid. Note that there are two advantages of implementation of the MUSIC: (1) the array Green's functions can be precalculated and stored for subsequent application; (2) the computation of the MUSIC spatial spectrum of equation 20 can be parallelized. Therefore, the MUSIC can be implemented very fast. In the MATLAB environment with a 3.2 GHz PC, the computation time of a two-object inversion of a TEMTADS data set is about $0.6 \sim 1.4$ minutes depending upon its iterative convergence speed. However, the computational time of the MUSIC for searching two objects of a TEMTADS data set is only 0.13 minutes.

APPLICATIONS

In this section, we present some evaluations of MUSIC-based source localization and imaging using the test-stand and the field data collected at Camp Butner, NC.

To demonstrate our methodology, we present the results mainly using TEMTADS (Nelson, 2008) data. TEMTADS is a new single-component multistatic system. It consists of a horizontally arranged coplanar array of 5×5 transmitters and receivers (Figure 1a) with a sensor footprint of 2×2 m. The sizes of its transmitters and receivers are 35×35 cm and 25×25 cm, respectively. It has 115 logarithmically spaced gates between 0.042 and 24.35 ms. For each transmitter excitation, TEMTADS records the response at all receivers. Thus it has spatial-temporal data of 625×115 at one static sounding location.

Test-stand data

This set of test-stand data was taken from a two-object configuration consisting of a $4.2''$ mortar + half shell. Figure 1b schematically shows the configuration in which the $4.2''$ mortar is horizontally centered 61 cm below the array and is kept stationary during the experiment. The clutter, consisting of a half shell at a depth 44 cm relative to the sensor in Figure 1b was moved horizontally at increments of 10 cm from 0 to 150 cm from the center of the array. A horizontal separation between the two objects is marked as H_d in the figure.

Figure 2 shows the data eigenvalues versus time when H_d is equal to 50 cm, $\cdots, 0$ cm. As shown earlier, the significant eigenvalues of D can be interpreted as those for the weighted polarizability tensor or as apparent principal polarizabilities. In these examples, we see six significant eigenvalues at larger horizontal separation ($H_d > 20$ cm). When the two objects are closely spaced, i.e., $H_d < 10$ cm, the gap between one set of significant eigenvalues and the noise is reduced. In these examples, the eigenvalue distribution indicates that there are two objects needed to produce the data.

To accurately estimate sources, we apply the MUSIC imaging technique to the data measured under these large and small separation configurations. In the imaging experiments, the scanning volume of $2 \times 2 \times 1$ m is discretized with intervals of $\Delta x = 0.05$ m, $\Delta y = 0.05$ m, and $\Delta z = 0.025$ m. The total scanning grids are $41 \times 41 \times 41 = 68921$. Given that data eigenvalue distribution, we choose $r = 6$ in equation 18 in the MUSIC evaluation. The sensor height was set at 0.175 m above the surface. For those easier scenarios, where separations between the objects are large, the MUSIC accurately localizes the two objects and a subsequent analysis is able to accurately recover the polarizabilities (not shown here). The more challenging scenario is to test whether we can recover the polarizations when the two objects are much closer. Our results are encapsulated in Figure 3, where the first two columns present the MUSIC 3D imaging and the last two columns the recovered polarizations using the imaging peak locations and the nonlinear inversion. In the following, we use subscripts "mu" and "nl" to denote source locations either obtained by the MUSIC imaging or the nonlinear inversion.

For the horizontal separation $H_d = 20$ cm (Figure 3a), the MUSIC derives the first peak location (marked as a cross on each imaging plot) at $\mathbf{r}_{mu,1} = (-0.20, 0.00, -0.31)$ m and the second peak at $\mathbf{r}_{mu,2} = (0.05, 0.00, -0.41)$ m. The imaging peak locations are very similar to those obtained by the nonlinear inversion: $\mathbf{r}_{nl,1} = (-0.22, -0.01, -0.31)$ m and $\mathbf{r}_{nl,2} = (0.03, -0.01, -0.40)$ m. Both sets of source locations are close to the ground truth locations shown in Figure 1b. Correspondingly, in the MUSIC and nonlinear inversion, one sees that one set of the recovered polarizations at $\mathbf{r}_2$ agrees well with the known polarizabilities of the $4.2''$ mortar. At $\mathbf{r}_1$, the three recovered polarizabilites decay fast and are distinct, indicating that it is a piece of clutter.

From the study in Song et al. (2011), an accurate polarizations recovery of smaller spatial separation between two objects is not impossible, but it can become difficult, particularly if two objects also have comparable polarization strength like the two-object case of the half shell and the $4.2''$ mortar in the test-stand data.

Figure 3b shows the MUSIC estimation when $H_d = 10$ cm, where it predicts the two objects at $\mathbf{r}_{mu,1} = (0.05, 0.00,$

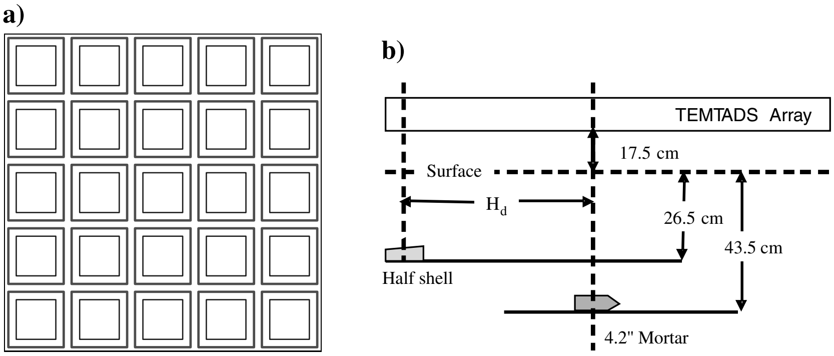

Figure 1. (a) TEMTADS: a single-component multistatic system consisting of a horizontally arranged coplanar array of 5×5 transmitters (thick line squares) and receivers (thin line squares). Each transmitter is 35×35 cm and each receiver 25×25 cm. (b) TEMTADS multiple-object measurement configuration: $4.2''$ mortar + half shell (deep and big clutter); H_d denotes a horizontal separation between the two objects.

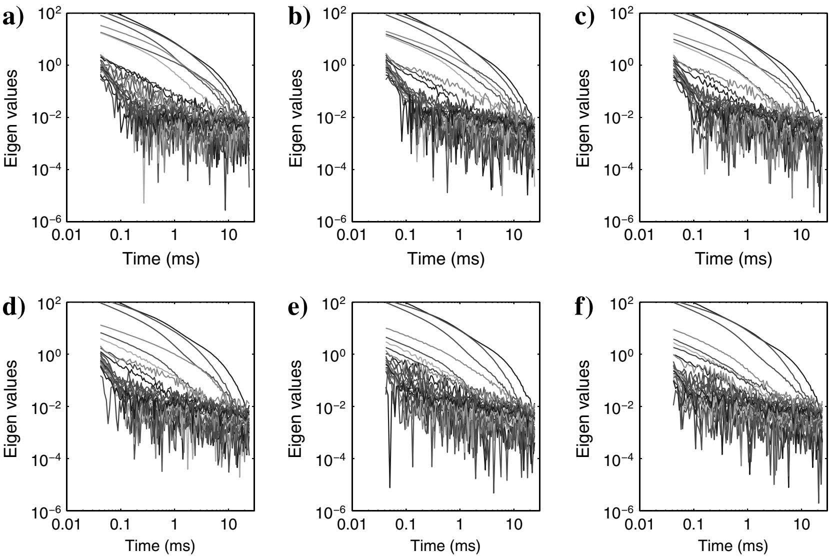

Figure 2. TEMTADS test-stand data example. Data eigenvalues. Mortar + HR at different horizontal separation: (a) $H_d = 50$ cm; (b) $H_d = 40$ cm; (c) $H_d = 30$ cm; (d) $H_d = 20$ cm; (e) $H_d = 10$ cm; (f) $H_d = 0$ cm.

−0.39) m and $\mathbf{r}_{mu,2} = (-0.15, 0.00, -0.31)$ m. Comparing with the true locations, $\mathbf{r}_1^{\text{true}} = (0.00, 0.00, -0.435)$ m and $\mathbf{r}_2^{\text{true}} = (-0.10, 0.00, -0.265)$ m, we see that all coordinates agree to within 5 cm and the polarizations of the objects are still well recovered. 4.2″ mortar can be clearly identified. The nonlinear inversion achieves the similar good performance shown at the fourth column of Figure 3b.

When $H_d = 0$ cm, i.e, the large piece of clutter is directly above the ordnance. The MUSIC algorithm results in Figure 3c estimates the peak locations at $\mathbf{r}_{mu,1} = (0.00, 0.00, -0.34)$ m and $\mathbf{r}_{mu,2} = (-0.10, 0.0, -0.34)$ m. This suggests there are two objects at the same depth and separated horizontally by 10 cm. On the other hand, the nonlinear inversion derives $\mathbf{r}_{nl,1} = (0.08, -0.01, -0.35)$ m and $\mathbf{r}_{nl,2} = (-0.10, -0.01, -0.35)$ m, but with a horizontal separation of about 18 cm. In terms of recovered polarization, the nonlinear inversion predicts two identical rod-like objects (Song et al., 2011). Nevertheless, the MUSIC results predict a rod-like object (one major polarizabiltiy and two equal minor polarizabilties) that matches most features of 4.2″ mortar, and a piece of clutter.

Field data

Here, we present some MUSIC examples applied to the test-pit data and field data collected at Camp Buter, NC for the ESTCP demonstration.

One set of the test-pit data was acquired with a single object, 105-HEAT, centered below the sensor array and oriented down. This is all the ground truth information available for this data set except the item depth. In Figure 4a, the data eigenvalue distribution indicates there are six eigenvalues that are above the noise level and they indicate the presence of two objects. Both objects have one major eigenvalue and two smaller, almost equal ones. The three dominant eigenvalue curves indicate that an object appears to be axially symmetric and has slow decay.

Turning to the MUSIC algorithm, we see that there are two predicted peak locations at $\mathbf{r}_{mu,1} = (0.05, 0.05, -0.58)$ m and $\mathbf{r}_{mu,2} = (0.00, 0.00, -0.29)$ m. Thus, there appears to be one deep and one shallow object that are nearly on top of each other. By treating this anomaly as a single-object at $\mathbf{r}_{mu,1}$ the recovered polarizabilties in Figure 4d show that the primary polarization is close to

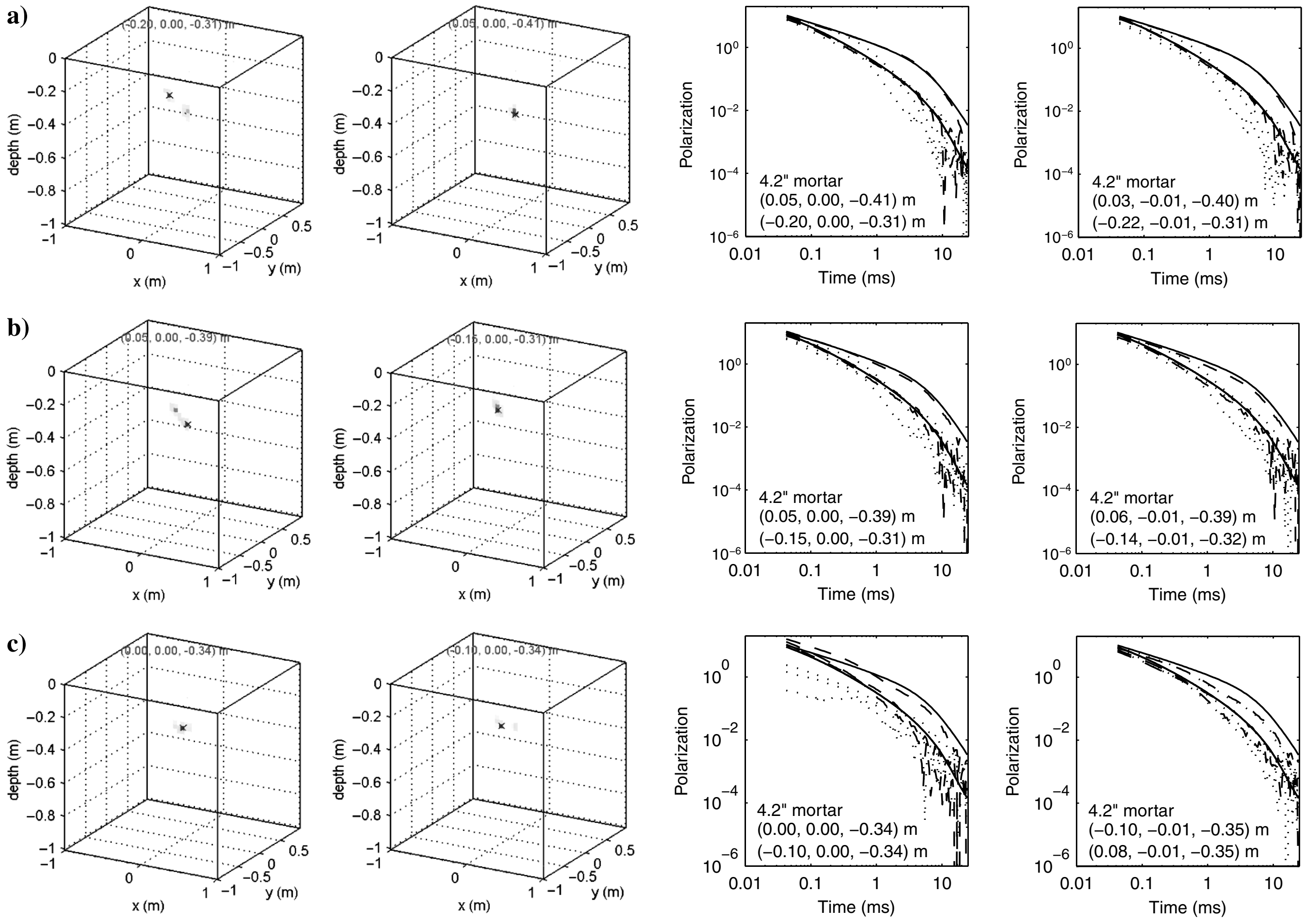

Figure 3. TEMTADS test-stand data example. MUSIC 3D spatial imaging (column 1 and 2) and recovered polarizabilities using imaging peak locations (column 3) and nonlinear inversions (column 4). Mortar + HR at different horizontal separation: (a) $H_d = 20$ cm; (b) $H_d = 10$ cm; (c) $H_d = 0$ cm. On each imaging plot, the peak location is denoted as a cross. On the polarization plots, the solid curves represent the known polarizabilities of 4.2″ mortar and the dashes and dots are the recovered polarizabilities.

that of the 105-HEAT, but the recovered secondary polarizations are larger and have different decay features. However, inverting as two objects at $\mathbf{r}_{mu,1}$ and $\mathbf{r}_{mu,2}$ provides two sets of polarizations. The polarization of the deep target agrees well with the known polarizabilities of 105-mm ordnance. The polarization of the shallow object has two equal major polarizabilities, accounting for the tail part of the 105-HEAT which is a plate-like object. The result shows that this big, vertically oriented object is appropriate to model as two objects.

As for the nonlinear inversion, a single-object model gives a source at $\mathbf{r}_{nl} = (0.03, -0.01, -0.46)$ m, and a two-object model $\mathbf{r}_{nl,1} = (0.03, -0.01, -0.58)$ m and $\mathbf{r}_{nl,2} = (0.03, -0.01, -0.30)$ m. A comparison of Figure 4g with Figure 4e, shows that the two sets of recovered polarizabilities from the two-object inversion are similar to those using the imaging peak locations, but the secondary polarizations of a source at $\mathbf{r}_{nl,1}$ are offset relative to the known secondary polarizabilities of the ordnance.

For the field data, we first examine one set of data marked as target 603 that arises from a small 37-mm projectile. The ground truth depth is 20 cm. In this example, the data eigenvalue distribution in Figure 5a indicates that there is one set of three significant curves whose dynamic pattern quite resembles the polarizabilities of 37-mm projectile. There seems another set of relatively smaller eigenvalues above the noise level. Using $r = 6$ and applying the MUSIC algorithm, we obtain two peak locations; one is at $\mathbf{r}_{mu,1} = (0.00, 0.20, -0.21)$ m, the other is on the edge of the area of interest at $\mathbf{r}_{mu,2} = (-0.75, -0.50, -0.11)$ m. Figure 5d shows the two sets of recovered polarizabilities: one at $\mathbf{r}_{mu,1}$ correctly identifies the ordnance and the other one at $\mathbf{r}_{mu,2}$ is likely a piece of munition fragment with a fast decay and is related to the set of three smaller eigenvalues in Figure 5a. The two-object inversion has a similar result with $\mathbf{r}_{nl,1} = (0.03, 0.21, -0.21)$ m and $\mathbf{r}_{nl,2} = (-0.79, -0.49, -0.00)$ m, as shown in Figure 5e. MUSIC and nonlinear inversion results mutually confirm and might indicate that there was likely a small piece of clutter around the measurement edge that data collectors missed.

The second example is a set of field data marked as target 62, arising from a 105 mm-HEAT. The ground truth depth is 62 cm. Figure 6a is the data eigenvalue plot in which there are three significant eigenvalues (one major one and two approximately equal secondary ones), visually showing similar decay behavior to the ground-truth polarizabilities of 105 mm. However, unlike the example of Figure 5, it is uncertain for this data set if there is another set of

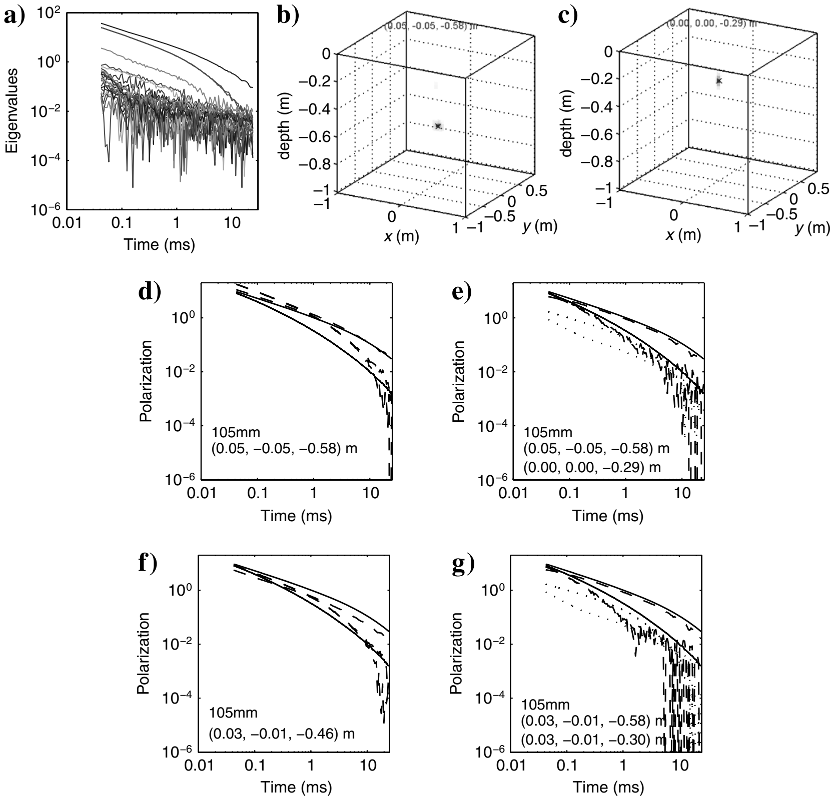

Figure 4. Camp Butner TEMTADS test-pit data example: (a) Data eigenvalues; (b and c) MUSIC 3D spatial imaging; (d and e) recovered polarizabilities using imaging peak locations; (f and g) recovered polarizabilities using the nonlinear single- and two-object inversions. On the polarization plots, the solid curves represent the known polarizabilities of 105 mm projectile and the dashes and dots the recovered polarizabilities.

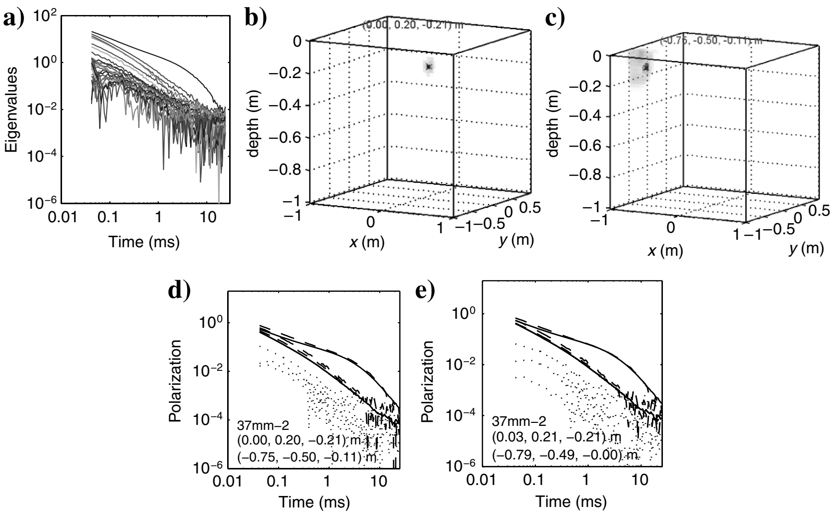

Figure 5. Camp Butner TEMTADS field data example. Target 603: (a) Data eigenvalues; (b and c) MUSIC 3D spatial imaging; (d) recovered polarizabilities using imaging peak locations; (e) recovered polarizabilities using the nonlinear inversion. On the polarization plots, the solid curves represent the known polarizabilities of 37-mm projectile and the dashes and dots are the recovered polarizabilities.

significant, even smaller eigenvalues among the noise eigenvalues. In the MUSIC application to this example, we still use $r = 6$.

Figure 6b and 6c shows the MUSIC 3D spatial imaging where the peak locations are at $\mathbf{r}_{mu,1} = (-0.10, 0.15, -0.56)$ m and $\mathbf{r}_{mu,2} = (-0.90, 0.15, -0.01)$ m. Using the peak locations, we solved a linear inverse problem and obtained the two sets of the polarizabilities for this target anomaly shown in Figure 6d. Applying the nonlinear inversion to this data set, we have the source locations at $\mathbf{r}_{nl,1} = (-0.10, 0.17, -0.50)$ m and $\mathbf{r}_{nl,2} = (-0.84, 0.27, -0.00)$ m and the corresponding recovered polarizabilities shown in Figure 6e.

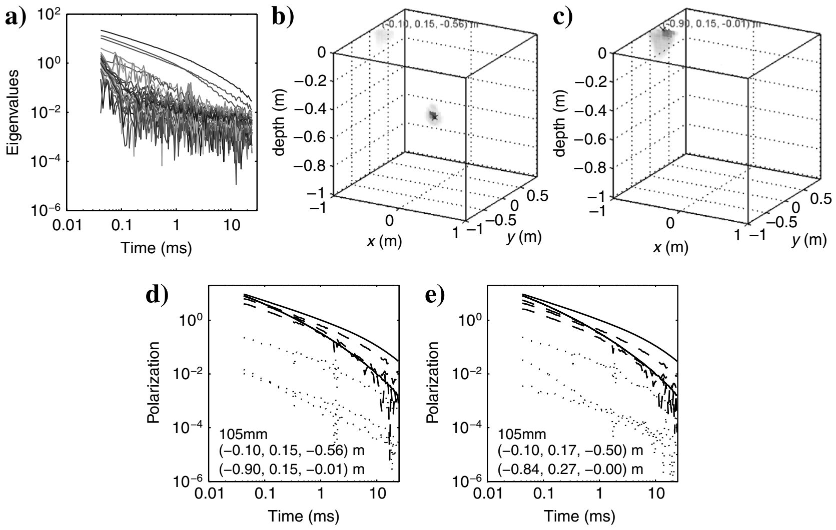

Figure 6. Camp Butner TEMTADS field data example. Target 62: (a) Data eigenvalues; (b and c) MUSIC 3D spatial imaging; (d) recovered polarizabilities using the imaging peak locations; (e) recovered polarizabilities using the nonlinear inversion. On the polarization plots, the solid curves represent the known polarizabilities of 105-mm projectile and the dashes and dots are the recovered polarizabilities.

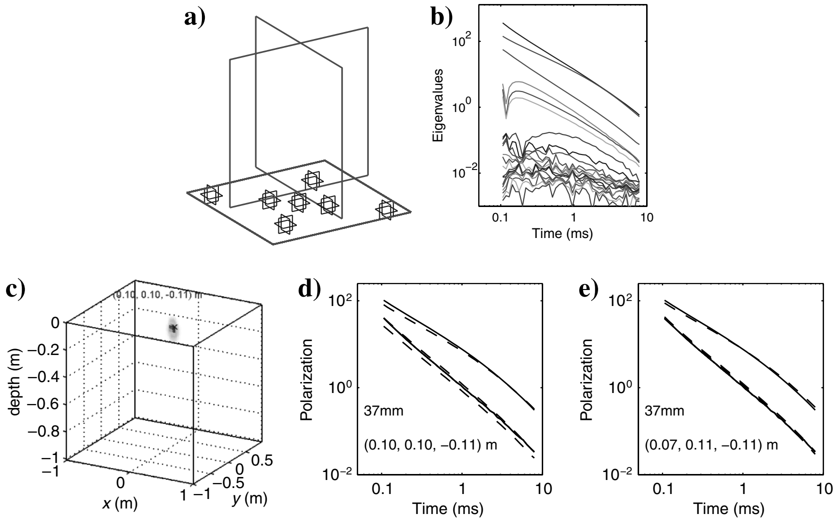

Figure 7. Camp Butner MetalMapper field data example. Target 130: (a) MetalMapper sensor configuration, a multicomponent system consisting of three orthogonal 1 × 1 m transmitters (large squares) and seven 3C receiver cubes (small squares) of 0.1 m; (b) data eigenvalues; (c) MUSIC 3D spatial imaging; (d and e) recovered polarizabilities using the imaging peak location and the nonlinear inversion. On the polarization plots, the solid curves represent the known polarizabilities of 37-mm projectile and the dashes are the recovered polarizabilities.

Comparing these two results, we observe that the MUSIC source locations are similar to those obtained from the nonlinear inversion. However, small differences in the two sets of locations appear to have an important impact for this example. Particularly for object 1, the MUSIC algorithm detects an object that is 6 cm deeper than the one derived in the nonlinear inversion, and it is closer to the array center. The use of the MUSIC peak locations recovers the polarizabilities that are much closer to the ground-truth polarizations than those recovered from the standard nonlinear inversion. Again, the edge anomaly predicted in both results might be likely ignored in the site record.

The final example is to show the application of MRM-based MUSIC technique to a data set from a system having a few transmitters and many receivers. As an introductory illustration of the principle, we choose the MetalMapper (Snyder et al., 2010) system with three orthogonal transmitters (roughly 1 × 1 m) and seven 3C receiver cubes of 0.1 m. Its configuration is given in Figure 7a. The sensor footprint is 1 × 1 m. The MetalMapper has 42 logarithmical time gates ranging from 0.106 to 7.91 ms. At one static sounding, the MetalMapper can record spatial-temporal data of 63 × 42.

A set of field data marked as target 130, arising from a 37 mm projectile, is used in this demonstration. The ground truth depth is given as 14 cm. Figure 7b is the data eigenvalues plotted in a receiver space where there are three significant eigenvalues (but not showing any axially symmetric feature) and others are treated as noise eigenvalues. In the MUSIC application to this example, we still use $r = 3$.

Figure 7c shows the MUSIC 3D spatial imaging where the peak location is at $\mathbf{r}_{mu} = (0.10, 0.10, -0.11)$ m. Using the peak location, we obtain the polarizabilities for this target anomaly shown in Figure 7d. Applying the nonlinear inversion to this data set, we have the source locations at $\mathbf{r}_{nl} = (0.07, 0.11, -0.11)$ m and the corresponding recovered polarizabilities shown in Figure 7e. Both methods achieve almost the identical results. Both recovered polarizations identify the ordnance correctly. This preliminary illustration supports the potential application of the MUSIC technique to a sensor system that has multiple receivers with a few transmitters.

CONCLUSIONS

We have established a 3D imaging technique to estimate the source locations of UXO based on the MUSIC principle for a multistatic EMI array. In the development, we introduce transmitter-based and receiver-based array operators that relate with the left and right singular vectors of a multistatic response matrix. A spatial metric function, which accounts for the vectorial nature of the problem and is designed for either both transmitter and receiver arrays or one array, is proposed to measure the projection of the computed signal subspace onto the noise subspace derived from data. A 3D source imaging of the metric function can be obtained by evaluating all potential locations over a region of interest. This is called the "MUSIC-type spatial spectrum" in which peaks are at or near where targets are present. Thus, they localize the objects in space. The joint diagonalization is used to effectively incorporate wideband multichannel responses in the imaging process.

The technique was evaluated using the test-stand and field data and compared with the nonlinear inversions. The results show that the MUSIC can be implemented very fast and perform the source localization with results comparable or superior to the iterative nonlinear inversion. This supports the position that the MUSIC can be a potential processing tool for multistatic sensors in addition to the standard nonlinear inversion. We also showed that the data eigenvalues of the MRMs are the eigenvalues of a weighted polarizability tensor or called "apparent principal polarizabilities." Thus, analysis of apparent principal polarizabilities might provide extra useful information about unknown targets.

We note that the MUSIC algorithm makes use of a projection of the array Green's functions onto a noise subspace to find sources. Determination of the dimension of the noise subspace or rank r plays an important role in the technique. This is related to quantifying the noise level and distribution characteristics of data eigenvalues. The detailed study and analysis about MUSIC algorithm sensitivity and stability with respect to a noise subspace remains to be explored.

ACKNOWLEDGMENTS

The authors would like to thank Daniel Steinhurst of Nova Research Inc. for providing with the test-stand data. We also are indebted to Mark Everett, Ivan Vasconcelos, D. Snyder, and the anonymous reviewer for their valuable remarks and suggestions that help improve our manuscript. This research was supported by a Strategic Environmental Research and Development Program Grant MM-1637.

REFERENCES

Bell, T., 2006, Adaptive and iterative processing techniques for overlapping signatures: AETC Inc., Arlington Virginia, Technical Report A855864, 1–16.

Bell, T. H., B. J. Barrow, and J. T. Miller, 2001, Subsurface discrimination using electromagnetic induction sensors: IEEE Transactions on Geoscience and Remote Sensing, **39**, 1286–1293, doi: 10.1109/36.927451.

Beran, L., and D. W. Oldenburg, 2008, Selecting a discrimination algorithm for unexploded ordnance remediation : IEEE Transactions on Geoscience and Remote Sensing, **46**, 2547–2557, doi: 10.1109/TGRS.2008.921394.

Billings, S. D., L. R. Pasion, L. Beran, N. Lhomme, L.-P. Song, D. W. Oldenburg, K. Kingdon, D. Sinex, and J. Jacobson, 2010, Unexploded ordnance discrimination using magnetic and electromagnetic sensors: Case study from a former military site: Geophysics, **75**, no. 3, B103–B114, doi: 10.1190/1.3377009.

Cardoso, J.-F., and A. Souloumiac, 1996, Jacobi angles for simultaneous diagonalization: SIAM Journal on Matrix Analysis and Applications, **17**, 161–164, doi: 10.1137/S0895479893259546.

Das, Y., J. E. McFee, J. Toews, and G. C. Stuart, 1990, Analysis of an electromagnetic induction detector for real-time localization of buried objects: IEEE Transactions on Geoscience and Remote Sensing, **28**, 278–288, doi: 10.1109/36.54354.

Devaney, A. J., 2005, Time reversal imaging of obscured targets from multistatic data: IEEE Transactions on Antennas and Propagation, **53**, 1600–1610, doi: 10.1109/TAP.2005.846723.

Gasperikova, E., J. T. Smith, H. Morrison, A. Becker, and K. Kappler, 2009, UXO detection and identification based on intrinsic target polarizabilities: Geophysics, **74**, no. 1, B1–B9, doi: 10.1190/1.2997419.

Golub, G. H., and C. F.V. Loan, 1989, Matrix computations, 2nd ed.: Johns Hopkins Press, 148.

Grant, F. S., and G. F. West, 1965, Interpretation theory in applied geophysics, section 6.5: McGraw-Hill Inc.

Grzegorczyk, T. M., B. Barrowes, F. Shubitidze, J. P. Fernández, I. Shamatava, and K. O'Neill, 2009, Detection of multiple subsurface metallic targets using EMI data: Proceedings of the SPIE, **7303**, 73030T–73030T10.

Horn, R. A., and C. Johnson, 1985, Matrix analysis: Cambridge University Press, 411–414.

Jackson, J. D., 1975, Classical electrodynamics, 2nd ed.: Wiley, 180–182.

Krim, H., and M. Viberg, 1996, Two decades of array signal processing research: The parametric approach: IEEE Signal Processing Magazine, **13**, 67–94, doi: 10.1109/79.526899.

Miller, J. T., T. Bell, J. Soukup, and D. Keiswetter, 2001, Simple phenomenological models for wideband frequency-domain electromagnetic induction: IEEE Transactions on Geoscience and Remote Sensing, **39**, 1294–1298, doi: 10.1109/36.927452.

Miller, J. T., D. Keiswetter, J. Kingdon, T. Furuya, B. Barrow, and T. Bell, 2010, Source separation using sparse-solution linear solvers: Proceedings of the SPIE, **7664**766409–1–766409–8.

Nelson, H. H., 2008, EMI array for cued UXO discrimination: ESTCP, MM-0601.

Pasion, L. R., 2007, Inversion of time domain electromagnetic data for the detection of unexploded ordnance: Ph.D. thesis, University of British Columbia.

Pasion, L. R., and D. Oldenburg, 2001, A discrimination algorithm for uxo using time domain electromagnetics: Journal of Environmental and Engineering Geophysics, **6**, 91–102, doi: 10.4133/JEEG6.2.91.

Schmidt, R. O., 1986, Multiple emitter location and signal parameter estimation: IEEE Antennas and Propagation Magazine, **34**, 276–280.

Shubitidze, F., B. Barrowes, K. O'Neill, I. Shamatava, and J. Fernandez, 2007, Combined NSMC and pseudospectral finite-difference method for inverting a buried object location: in Proceedings: Symposium on the Application of Geophysics to Engineering and Environmental Problems, 1475–1484.

Shubitidze, F., D. Karkashadze, J. P. Fernández, B. E. Barrowes, K. O'Neill, T. M. Grzegorczyk, and I. Shamatava, 2010, Applying a volume dipole distribution model to next-generation sensor data for multiobject data inversion and discrimination: Proceedings of the SPIE, **7664**, 7664071–76640711.

Smith, J. T., and H. F. Morrison, 2004, Estimating equivalent dipole polarizabilities for the inductive response of isolated conductive bodies: IEEE Transactions on Geoscience and Remote Sensing, **42**, 1208–1214, doi: 10.1109/TGRS.2004.826789.

Snyder, D. D., D. George, S. C. MacInnes, and J. T. Smith, 2008, An assessment of three dipole-based programs for estimating UXO target parameters with induction EM: 78th Annual International Meeting, SEG, Expanded Abstracts, 2902–2906.

Snyder, D. D., M. Prouty, S. Jose, D. C. George, T. King, Z. Blackhawk, M. Poulton, and A. Szidarovszky, 2010, Discrimination at Camp San Luis Obispo with the MetalMapper: Symposium on the Application of Geophysics to Engineering and Environmental Problems, 1–16.

Song, L.-P., D. W. Oldenburg, L. R. Pasion, and S. D. Billings, 2008, Adaptive focusing for source localization in EMI sensing of metallic objects: A preliminary assessment: Journal of Environmental and Engineering Geophysics, **13**, 131–145, doi: 10.2113/JEEG13.3.131.

Song, L.-P., D. W. Oldenburg, L. R. Pasion, and S. D. Billings, 2009, Transient electromagnetic inversion of multiple targets: Proceedings of the SPIE, **7303**, 73030R–73030R12.

Song, L.-P., L. R. Pasion, S. D. Billings, and D. W. Oldenburg, 2011, Nonlinear inversion for multiple objects in transient electromagnetic induction sensing of unexploded ordnance: Technique and applications: IEEE Transactions on Geoscience and Remote Sensing, **49**, 4007–4020, doi: 10.1109/TGRS.2011.2132138.

Van Veen, B. D., and K. M. Buckley, 1988, Beamforming: A versatile approach to spatial filtering: IEEE Signal Processing Magazine, **5**, 4–24.

Wax, M., and J. Sheinvald, 1997, A least-squares approach to joint diagonalization: IEEE Signal Processing Letters, **4**, 52–53, doi: 10.1109/97.554471.

Zhang, Y., L. Collins, C. B. H. Yu, and L. Carin, 2003, Sensing of unexploded ordnance with magnetometer and induction: Theory and signal processing: IEEE Transactions on Geoscience and Remote Sensing, **41**, 1005–1015, doi: 10.1109/TGRS.2003.810922.